

TESTING NUMERICAL MODELS OF SIMPLE CRATER FORMATION G. S. Collins, Impacts and Astro-materials Research Centre, Dept. Earth Science & Eng., Imperial College London, SW7 2AZ, UK (g.collins@imperial.ac.uk).

Introduction: Recent improvements to the iSALE shock physics code for simulating impacts allow more rigorous comparison of numerical model predictions with geological and geophysical observations [1]. Here numerical models of simple crater formation on Earth and the Moon are tested against observational constraints derived from drill core data [2], Bouguer gravity anomalies [e.g., 3] and structural observations [e.g., 4]. Although simple crater formation is already relatively well understood [5], these numerical simulations provide new insight into porosity generation and structural deformation in the rim area and a test for existing geometric models [6].

Method: Numerical simulations of simple crater formation were performed using iSALE [1,7,8] for typical impact conditions on Earth and the Moon. Impacts on Earth assumed an impactor diameter of 100-250 m, an impact velocity of 15 km/s and a surface gravity of 9.81 m/s^2 ; impacts on the Moon assumed the same impact velocity, an impactor diameter of 1-2 km and a surface gravity of 1.63 m/s^2 . In all simulations the impactor and target were modeled using a material model for granite. The granite thermodynamic equation of state table was generated using ANEOS, while material strength was modeled using the approach described in [8]. In all simulations the initial target was assumed to have zero porosity. Porosity generation by shear deformation was calculated using a new dilatancy model [1], with parameters appropriate for pre-fractured rock masses. Bouguer gravity anomalies were computed from the post-impact porosity distribution beneath the simulated crater.

Gravity and density anomaly: Numerical model predictions of density changes beneath simple craters can be compared with observed gravity and porosity anomalies [1]. Figure 1 shows that the Bouguer gravity anomaly produced by a simulated 4-km diameter terrestrial simple crater compares well with the observed Bouguer gravity anomaly at Brent, Canada [6]. Post-impact filling of pore-space by water or compaction by burial are not accounted for in the model and would reduce the synthetic gravity anomaly magnitude; however, this could be compensated for by a small increase in the assumed maximum dilatancy angle.

Simple crater geometry: Fresh lunar simple craters share a common depth-diameter ratio of $\sim 1:5$. A synthesis of terrestrial simple crater observations suggests further geometrical similarity between simple craters. Breccia lens thickness is typically equal to the apparent crater depth and final crater rim height is approximately one twentieth of the final rim diameter [6]. Numerical simulations of simple crater formation with dilatancy are consistent with these geometrical constraints (Fig. 1). Dilatant behavior is important to rep-

licate the thickness of the breccia lens owing to both the increase in volume and the reduced strength of the dilated breccia lens material. Simulations that neglect dilatancy produce a breccia lens that is too thin and a final crater that is too deep.

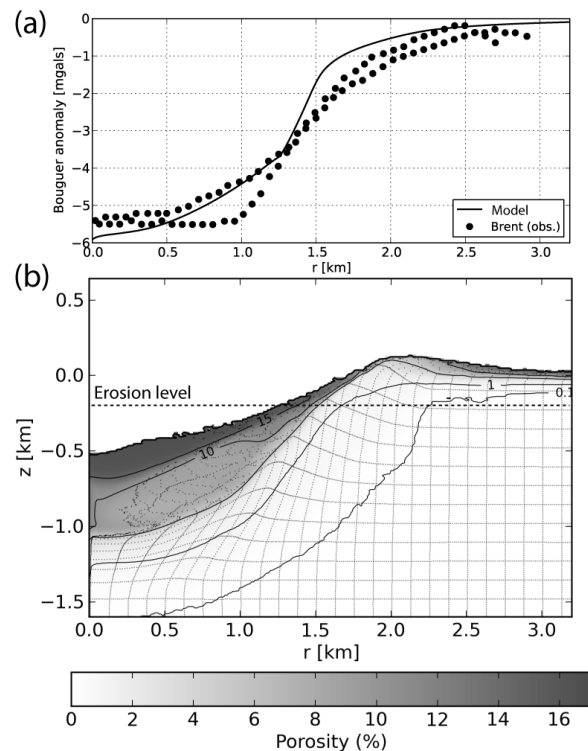


Figure 1 Comparison of numerical model predictions of Brent simple crater formation with observed gravity anomaly [6]. The comparison assumes a present-day erosion level 200-m below the preimpact surface and a postimpact sedimentary infill relative density of -0.17 g/cc [1]. Shading shows subcrater distribution of porosity; contours delineate 0.1, 1, 5, 10 and 15% porosity levels.

Rim formation: Recent observations of layered outcrops in the rims of lunar simple craters and small complex craters provide new constraints on rim formation [4]. Importantly, these measurements suggest that the elevated crater rim is caused predominantly by structural uplift of rocks surrounding the crater, with ejecta deposition accounting for only $\sim 20\%$ of the total rim height above the preimpact surface [4]. Numerical simulations of simple crater formation provide insight into the mechanism of rim formation and allow observations at the rim to be extrapolated outward beneath the continuous ejecta blanket (Figs 2 and 3).

The 5% porosity contour (Fig. 1) provides a good proxy for the “true crater” [5,6], which divides the (para)autochthonous rocks of the crater floor, walls and rim (below red line) from the allochthonous ejecta and breccia that form the debris lens and continuous

ejecta deposit (above red line). Using this boundary and Lagrangian tracer particles it is possible to distinguish four units involved in simple crater formation (Figs. 2 and 3): the structurally *uplifted rim* (and walls); the *breccia* (debris) *lens*; the *ejecta curtain*, which lands to form the continuous ejecta blanket; and the overturned *ejecta flap*, which drapes over the uplifted structural rim.

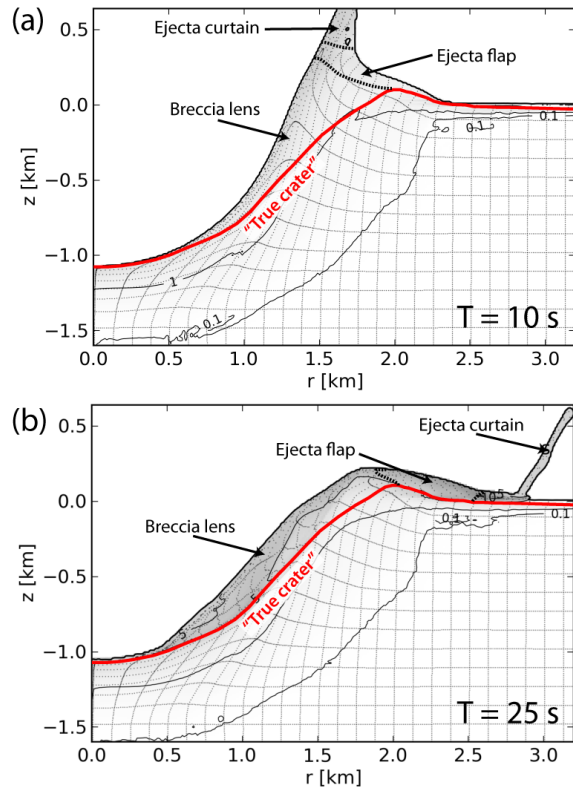


Figure 2 Development of breccia lens and proximal ejecta deposit: (a) transient crater forms after approximately 10 seconds; (b) at 25 s the walls of the transient crater collapse inward to form breccia lens, the ejecta curtain lands to form the continuous ejecta blanket, and the overturning ejecta flap drags outward over the uplifted rim. Shading and contour lines show subcrater porosity (see Fig. 2 for scale).

Numerical simple crater simulations reveal a complex rim formation process. Structural uplift, driven by the subterranean portion of the excavation flow field extends only as far as $\sim 1.25R$ (where R is the final rim radius; Fig. 3c) and is established by the approximate time of transient crater formation (Fig. 2a, 3b). Ejecta within the *ejecta curtain* at this time will land at radial distances $r > 1.25R$, beyond the zone of structural rim uplift. At the base of the ejecta curtain is the *ejecta flap*, a complex zone separating the outwardly moving *ejecta curtain* from the inwardly collapsing *breccia lens*. The flap overturns and drags outward over the *uplifted rim*, before draping its outer flank (Fig. 2b).

Consistent with observations of fresh lunar craters [4], the structure of the final crater rim is dominated by structural rim uplift: total rim height is $\sim 75\%$ structural

uplift and $\sim 25\%$ ejecta (flap) thickness. However, this ratio is not constant with increasing radial distance: the limited radial extent of the structural uplift implies that outside $1.25R$ elevated topography is almost entirely related to ejecta thickness. Hence, although structural rim uplift is the dominant contribution to rim elevation it is a minor contribution to the total volume of elevated topography. The latter is dominated by ejecta from the excavated cavity (Fig. 3a; green), which derives from a maximum depth of $\sim 0.1D_{tc}$ (where D_{tc} is the transient crater diameter), consistent with many independent constraints on ejecta provenance.

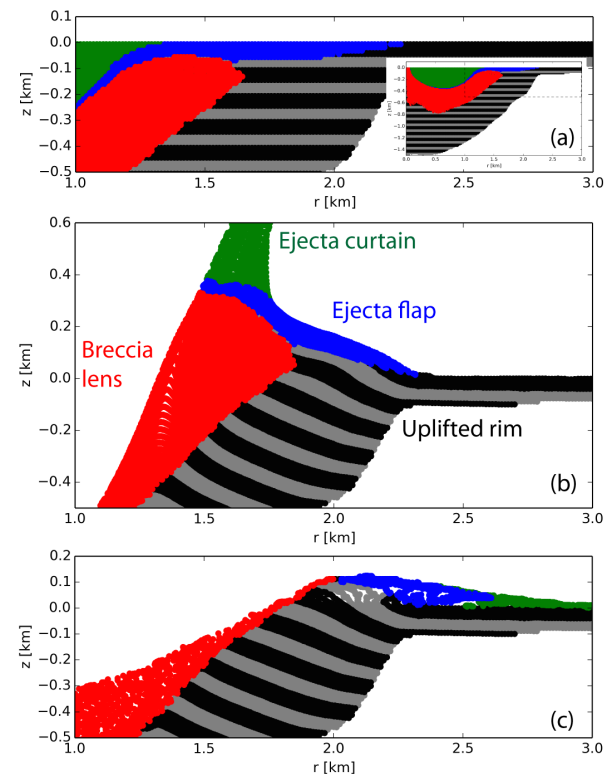


Figure 3 Position of different crater units in the vicinity of the crater rim (breccia lens, ejecta curtain, ejecta flap, uplifted rim) before, during and after impact: (a) initial position (provenance); (b) position at time of transient crater formation ($T = 10$ s); (c) final location. Structural deformation is shown for the uplifted rim by grey and black layers—note: uplifted rim makes the dominant contribution to rim height (c). Inset in (a) shows the full provenance map for context—note: the maximum ejecta depth (green) is $0.35 \text{ km} \approx 0.1D_{tc}$.

Acknowledgements I gratefully acknowledge the developers of iSALE (www.isale-code.de/iSALE) and funding from STFC grant: ST/J001260/1.

References [1] Collins GS (2014) *JGR Planets*, doi: 10.1002/2014JE004708. [2] Innes MJS (1961) *JGR Solid Earth*, 66(7), 2225–2239. [3] Pilkington M and Grieve RAF (1992) *Rev. Geophys.* 30(2): 161–181. [4] Sharpton VL (2014) *JGR Planets* 119, 2013JE004523 (2014). [5] Grieve RAF and Garvin JB (1984) *JGR Solid Earth* 89, 11561–11572. [6] Grieve RAF et al. (1989) *Meteoritics*, 24(2), 83–88. [7] Wünnemann K et al. (2006) *Icarus*, 180, 514–527. [8] Collins GS et al. (2004) *MAPS*, 39, 217–231.